

# Atomic Resolution Imaging of Nanoscale Chemical Expansion in $\text{Pr}_x\text{Ce}_{1-x}\text{O}_{2-\delta}$ during *In Situ* Heating

Jessica G. Swallow,<sup>†</sup> Ja Kyung Lee,<sup>‡</sup> Thomas Defferriere,<sup>†</sup> Gareth M. Hughes,<sup>‡</sup> Shilpa N. Raja,<sup>†</sup> Harry L. Tuller,<sup>†</sup> Jamie H. Warner,<sup>\*,‡,†</sup> and Krystyn J. Van Vliet<sup>\*,†</sup>

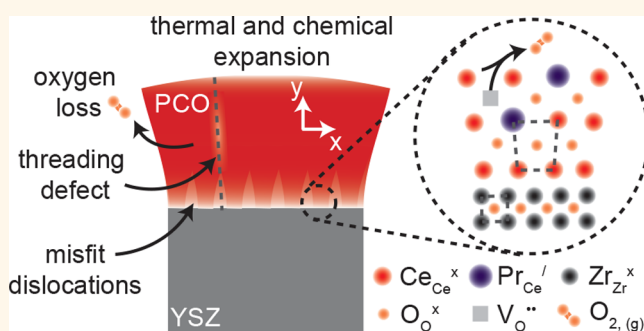
<sup>†</sup>Department of Materials Science and Engineering, Massachusetts Institute of Technology, Cambridge, Massachusetts 02139, United States

<sup>‡</sup>Department of Materials, University of Oxford, Oxford OX1 3PH, United Kingdom

## S Supporting Information

**ABSTRACT:** Thin film nonstoichiometric oxides enable many high-temperature applications including solid oxide fuel cells, actuators, and catalysis. Large concentrations of point defects (particularly, oxygen vacancies) enable fast ionic conductivity or gas exchange kinetics in these materials but also manifest as coupling between lattice volume and chemical composition. This chemical expansion may be either detrimental or useful, especially in thin film devices that may exhibit enhanced performance through strain engineering or decreased operating temperatures. However, thin film nonstoichiometric oxides can differ from bulk counterparts in terms of *operando* defect concentrations, transport properties, and mechanical properties. Here, we present an *in situ* investigation of atomic-scale chemical expansion in  $\text{Pr}_x\text{Ce}_{1-x}\text{O}_{2-\delta}$  (PCO), a mixed ionic–electronic conducting oxide relevant to electrochemical energy conversion and high-temperature actuation. Through a combination of electron energy loss spectroscopy and transmission electron microscopy with *in situ* heating, we characterized chemical strains and changes in oxidation state in cross sections of PCO films grown on yttria-stabilized zirconia (YSZ) at temperatures reaching 650 °C. We quantified, both statically and dynamically, the nanoscale chemical expansion induced by changes in PCO redox state as a function of position and direction relative to the film–substrate interface. Additionally, we observed dislocations at the film–substrate interface, as well as reduced cation localization to threading defects within PCO films. These results illustrate several key aspects of atomic-scale structure and mechanical deformation in nonstoichiometric oxide films that clarify distinctions between films and bulk counterparts and that hold several implications for *operando* chemical expansion or “breathing” of such oxide films.

**KEYWORDS:** chemical expansion, nonstoichiometric oxide, *in situ* transmission electron microscopy, chemomechanics, thin film, defects



Nonstoichiometric oxides that support very large point defect concentrations are active materials in diverse applications including solid oxide fuel cells (SOFCs), electrolyzers, high-temperature oxide actuators, catalysts, and gas sensors.<sup>1–4</sup> Generally, the point defects that provide the *nonstoichiometry* in these materials are oxygen vacancies that foster important functional properties including fast ionic conductivity and/or oxygen exchange kinetics. Formation, annihilation, and migration of these defects also tend to be coupled to material volume, manifest as chemical expansion or lattice volume coupled to defect content. Chemical expansion is a well-known feature of many nonstoichiometric oxides including fluorites, perovskites, and Ruddlesden–Popper phases.<sup>5–7</sup> It is often cited as a source of mechanical failure

because it can produce undesired stress or strain in layered systems *in situ*.<sup>8</sup> Such chemomechanical coupling need not always be a negative effect, however. In fact, electrochemically stimulated chemical expansion in such oxides can be used for high-temperature actuation in extreme environments.<sup>2</sup> Further, in some cases, this volume coupled to chemistry may be used to improve device performance, for example, by using tensile strain to decrease oxygen vacancy formation energies and thereby enhance exchange kinetics or diffusivity.<sup>9–11</sup> This concept, known as strain engineering, has the potential to

Received: October 31, 2017

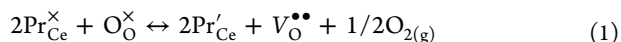
Accepted: January 16, 2018

Published: January 16, 2018

decrease the operating temperature of thin film SOFCs or related devices without sacrificing energy conversion efficiency.<sup>12</sup> In fact, the use of thin film nonstoichiometric oxides extends beyond electrochemical energy conversion and storage applications; resistive switches and gas separation membranes may also benefit from miniaturized dimensions.<sup>4,13</sup>

Leveraging or engineering such chemical expansion effects *in situ*, particularly for applications including strain-engineered SOFC cathodes or high-temperature oxide actuators, requires detailed understanding of how stress and strain develop near mechanically constrained interfaces *in situ*. Both the uniformity and magnitude of such effects are important, especially at length scales <100 nm that describe line defect contributions to deformation and the elementary steps of charge or mass transfer in the atomic lattice. Here, we characterized *in situ* the atomic-scale response of a nonstoichiometric oxide film to elevated temperature up to 650 °C and distinct oxidation states, through high-resolution transmission electron microscopy (TEM) and electron energy loss spectroscopy (EELS). This nonstoichiometric oxide, Pr-doped ceria or Pr<sub>x</sub>Ce<sub>1-x</sub>O<sub>2-δ</sub> (PCO), holds particular promise for high-temperature oxide actuators because it exhibits large chemical strain coupled to relatively modest applied voltages (~0.1% strain per 100 mV) at temperatures above 550 °C.<sup>2</sup> A model mixed ionic–electronic conducting oxide, PCO has been well-characterized in terms of defect chemistry, oxygen exchange kinetics, chemical expansion coefficient, and elastic properties.<sup>6,14–16</sup> PCO exhibits the fluorite crystal structure widely used in SOFC and oxygen storage applications and a large chemical expansion coefficient of 0.087 (Δε/Δδ).<sup>6</sup> Therefore, PCO is an ideal model system for understanding thin film chemical expansion effects at the atomic scale.

Equation 1 describes the oxygen vacancy formation reaction in the model nonstoichiometric oxide material Pr<sub>x</sub>Ce<sub>1-x</sub>O<sub>2-δ</sub> (PCO) using Kröger-Vink notation, where Pr<sub>Ce</sub><sup>x</sup> and Pr<sub>Ce</sub><sup>'</sup> denote Pr<sup>4+</sup> and Pr<sup>3+</sup>, respectively, on Ce sites, O<sub>O</sub><sup>x</sup> denotes O<sup>2-</sup> on an oxygen site, and V<sub>O</sub><sup>••</sup> denotes a net double positively charged vacancy on an oxygen site:



Equation 1 exemplifies the oxygen vacancy formation reactions that occur in conjunction with chemical expansion in most nonstoichiometric oxide materials. Increased volume arises from the increased size of the two reduced cations on the right side of eq 1, despite the slight volumetric contraction that occurs around the oxygen vacancy.<sup>17</sup> In general, increased charge localization to these cations can be expected to increase the chemical expansion coefficient α<sub>c</sub> that couples chemical strain ε to change in oxygen vacancy concentration Δδ according to eq 2, suggesting that it may be possible to tune this coefficient by cation substitution.<sup>18</sup>

$$\epsilon = \alpha_c \Delta\delta \quad (2)$$

The coefficient α<sub>c</sub> is assumed generally to be independent of temperature, but this is not always the case.<sup>5</sup> Additionally, the value of α<sub>c</sub> can vary between bulk and thin film forms of the same oxide and may be anisotropic.<sup>6,19–22</sup>

Thin films exhibit two important differences from bulk counterparts of the same material: (1) relatively higher densities of crystallographic defects and (2) influence of mechanical constraints at the film–substrate interface. These differences hold particular importance in nonstoichiometric

oxide films such as Pr-doped CeO<sub>2</sub> considered herein. The potential for higher defect density in thin films is attributed generally to the relative contribution of surfaces and interfaces, which naturally comprise a larger proportion of material volume in thin film specimens. For example, TEM and EELS experiments have shown that CeO<sub>2</sub> films and nanoparticles can exhibit especially large oxygen vacancy concentrations near free surfaces or exhibit regions enriched in reduced cations in space-charge layers at grain boundaries or interfaces.<sup>23–25</sup> Furthermore, additional capacity for inducible film stress due to thermal or chemical stimuli is attributed to the fact that films adhered to substrates are constrained from lateral displacement and strain at the film–substrate interface. At the atomic scale, this constraint can also include strain associated with film deposition, including atomic lattice mismatch between the two materials. In the context of thermal and chemical expansion, this constraint of lateral displacement with respect to bulk forms of the same material induces additional film strain (or stress) that depends on relative magnitude of thermal or chemical expansion coefficients describing lattice parameter changes as a function of temperature *T* or point defect content, respectively.

Nonstoichiometric oxide films can also exhibit lattice strain as the point defect content changes *in situ*, including changes in concentrations of reduced cations and corresponding oxygen vacancies. Interfacial constraint may cause most of this environment-dependent lattice strain to occur perpendicular to the interface. This anisotropy in lattice parameter as a function of distance from the film–substrate interface could result plausibly in anisotropic physical and mechanical properties including charge transport and elastoplastic properties. It is of interest to determine to what extent stress-relief mechanisms, such as anisotropic chemical strain, line defect motion, or phase separation, occur and contribute to nonstoichiometric oxide films at high temperatures. Such direct observations are important particularly to discern whether linear defects, phase changes, or spatially anisotropic strains may also couple to other important functional properties of these oxides.

Atomic-resolution electron microscopy can provide such a direct means of characterizing chemical expansion *in situ*.<sup>26,27</sup> There are two main types of atomic-resolution electron microscopy, each with distinct advantages, that are of interest for this purpose, specifically phase contrast TEM and scanning transmission electron microscopy (STEM). The resolution of these techniques has been improving steadily, especially with recent developments in aberration correction, such that atomic columns can be resolved.<sup>28,29</sup> STEM is often available in combination with EELS that can be used to identify elemental composition as well as oxidation states.<sup>30–32</sup> Atomic-resolution images enable local lattice strain detection through a combination of selected area diffraction and geometric phase analysis (GPA, translation of local fast Fourier transform (FFT) information throughout an image to identify strain states relative to a user-specified reference state<sup>33</sup>). Because chemical expansion is characterized by both a change in lattice parameter and a change in oxidation state, high-resolution STEM with EELS provides a powerful method of characterizing this effect at the atomic level.<sup>33,34</sup>

PCO exhibits both chemical expansion and key discrepancies between film and bulk properties. For example, PCO films exhibit higher oxygen vacancy concentrations than bulk counterparts of the same nominal composition under the

same operating conditions.<sup>35</sup> PCO films grown on yttria-stabilized zirconia (YSZ, a common choice of SOFC electrolyte) have exhibited irreversible stress relaxation at high temperature that is not yet explained fully.<sup>20</sup> Additionally, PCO films have shown a stronger dependence of Young's elastic modulus  $E$  on temperature and oxygen partial pressure  $pO_2$  than expected based on modeling of bulk PCO or inferred from measurements of the related oxide  $Gd_xCe_{1-x}O_{2-\delta}$ .<sup>16</sup> Specifically,  $E$  decreased with increased  $T$  and decreased oxygen partial pressure  $pO_2$  as the oxide exhibited thermal and chemical expansion, an effect that could be magnified by both increased changes in reduced cation content (and/or associated oxygen vacancy content  $\delta$ ) for a fixed change in environmental conditions or anisotropic chemical strain resulting from constrained deformation. Thus, PCO films grown on YSZ substrates (as we analyzed in the current study) can be expected to exhibit microstructural and nanoscale features that facilitate these observations and may be observed with high-temperature atomic-resolution microscopy.

Several previous studies of undoped and Pr-doped  $CeO_2$  at room temperature have been conducted by TEM, STEM, and EELS. Sheth *et al.* reported that PCO films grown by pulsed laser deposition (PLD) on YSZ substrates exhibited partial epitaxy with threading dislocations observable *via* TEM that propagated from the interface to the (100)-oriented film surface.<sup>20</sup> Those authors also reported irreversible stress relaxation observed by multibeam optical stress sensors at high temperature for which the mechanisms were not elucidated.<sup>20</sup> Several groups have reported misfit dislocations in  $CeO_2$  films grown epitaxially on YSZ.<sup>24,36,37</sup> Sinclair *et al.* also noted that substantial electron beam exposure for very thin ( $\sim 11$  nm)  $CeO_2$  membranes induced vacancy ordering and sample reduction that could be recovered readily with reoxidation of the sample.<sup>36</sup> Vacancy ordering can also be induced in  $CeO_2$  films at room temperature by application of volt-scale electrical bias, a type of *in situ* TEM that recently has been applied to the study of resistive switching effects in nonstoichiometric oxide materials at room temperature.<sup>32,38,39</sup>

Others have also reported nonuniform composition or oxidation state in close proximity to grain boundaries, interfaces, and surfaces in doped and undoped  $CeO_2$  at room temperature.  $CeO_2$  nanoparticles exhibited large vacancy concentrations, surface rearrangements, and lattice expansion that could reach up to 7% after sample reduction in hydrogen at high temperatures, an effect that may be enhanced by doping.<sup>26,40</sup> Room temperature STEM imaging of  $CeO_2$  films grown on YSZ with EELS has shown substantial Ce cation reduction within a 5 nm distance from the interface, consistent with the concept of interfacial space charge.<sup>24</sup> Enhanced cation reduction has also been observed within grain boundary cores in sintered Gd/Pr codoped  $CeO_2$  powders, along with Gd and Pr enrichment at grain boundaries. This observation was correlated with reduced migration energies for oxygen vacancies, representing an important way in which local microstructural features may be used to enhance functional properties (*e.g.*, ionic conductivity) by providing fast-conduction pathways.<sup>41</sup> In that case, cation reduction at the grain boundary was concurrent with depleted oxygen content, indicating that this was not a space-charge effect. Opposite effects might exist proximal to dislocations in doped or undoped  $CeO_2$ ; computational results have indicated that edge dislocations could retard oxide ion diffusion by causing segregation of charged defects.<sup>42</sup> While those prior studies

observed or predicted many types of nonuniform composition or oxidation states in  $CeO_2$  at room temperature, little direct evidence of these effects at high temperatures has been gathered. Further, the correlation of these defect distributions with chemical expansion has been explored only minimally. In fact, while volume-averaged chemical expansion has been observed by diffraction, stress measurements, or probe-based approaches, there exist few reports of defect distribution or chemical expansion at film–substrate interfaces.<sup>27</sup>

Here we present analysis of defects and displacements in a model PCO–YSZ system, using an *in situ* heating holder with TEM, STEM, and EELS to quantify chemical expansion, composition, and oxidation state of film–substrate cross sections. We analyzed two cross sections, one imaged exclusively at room temperature (sample A) and one imaged using the *in situ* heating holder at temperatures up to 650 °C (sample B). As shown schematically in Figure 1, we focused

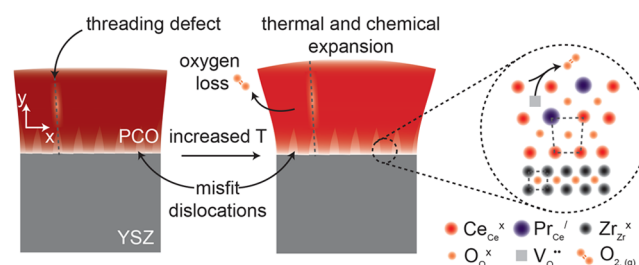


**Figure 1.** Schematic of *in situ* TEM experiments on non-stoichiometric oxide film cross sections. Epitaxial  $Pr_{0.1}Ce_{0.9}O_{2-\delta}$  (PCO) films grown on yttria-stabilized zirconia (YSZ) substrates subject to mechanical constraint at interface. Upon heating inside microscope, PCO films exhibit anisotropic thermal and chemical expansion and associated sample reduction (indicated by lighter film color) through oxygen loss. Defects at interface between the film and/or threading throughout the film thickness may contain higher concentrations of reduced cations. PCO strain determined through Fourier transform analysis of electron microscopy images, and oxidation state change identified by electron energy loss spectroscopy.

particular attention to the role of the interfacial constraint, modes of chemical expansion accommodation within the defective lattice, and the nature of linear defects that emerge upon film oxidation. These results confer important implications for understanding how epitaxial nonstoichiometric oxide films may respond to interfacial stresses arising from thermal or chemical expansion *operando*, including potential impact on charge transport or reactivity relevant to high-temperature actuation or electrochemical energy conversion.

## RESULTS AND DISCUSSION

**Structural Characterization of As-Grown PCO.** We first characterized PCO–YSZ film–substrate cross sections at room temperature to assess as-deposited PCO microstructure. Figure 2a shows a low-magnification TEM image of the PCO–YSZ cross section (sample A). The film (with an initial thickness of  $\sim 200$  nm measured by profilometry) exhibited apparently columnar microstructure. However, upon closer inspection, the threading defects propagating from the interface to the surface of the film (highlighted by white arrows) were discerned to be disordered regions and not grain boundaries separating grains of distinct orientations. Distinct grain orientations would appear as rotated or distorted FFT patterns, while doubled

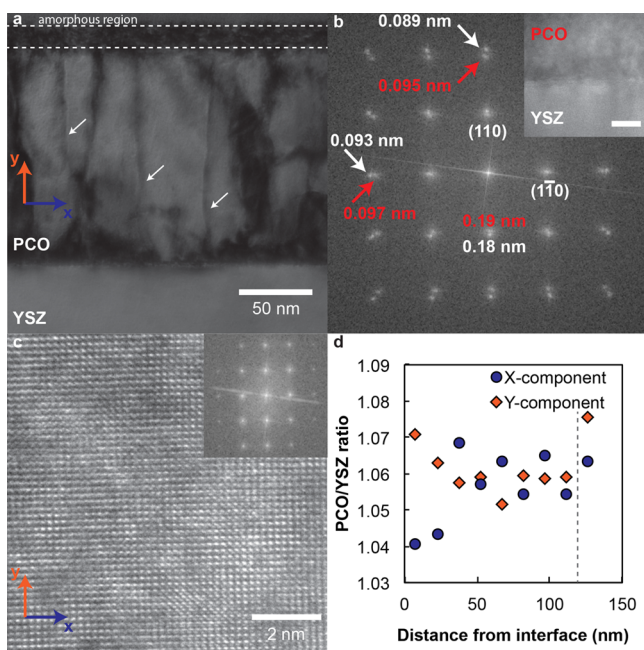


**Figure 2.** (a) Low-magnification TEM image of  $\text{Pr}_{0.1}\text{Ce}_{0.9}\text{O}_{2-\delta}$  (PCO) film on yttria-stabilized zirconia (YSZ) substrate cross section at room temperature. Threading features propagating from the YSZ interface to the surface are highlighted by white arrows. The focused ion beam preparation resulted in a disordered and reduced “surface layer” separated by dashed lines. (b) Fast Fourier transform of the PCO–YSZ interface (inset, 5 nm scale bar) showing doubled reflections indicative of epitaxy. Red arrows denote PCO spots, and white arrows denote YSZ spots. Sample tilt accounts for slight FFT pattern asymmetry. (c) High-resolution ADF-STEM image of PCO film showing atomic resolution and coordinate system (inset, FFT of this region). Lattice spacing parallel to ( $x$ ) and normal to ( $y$ ) the film–substrate interface indicated by blue and orange, respectively. (d) Ratio of PCO lattice spacing to YSZ as a function of distance from the interface, demonstrating expected  $\sim 6\%$  mismatch and anisotropic strain within 30 nm of the interface.

spots at the same orientation but slightly differing spacing  $d$  indicate epitaxy. We found no evidence of grain rotation or mismatch on either side of these defects; instead the film was oriented in a consistently epitaxial manner extending along the  $y$ -axis from the interface toward the free surface of the deposited films. The doubled spots in the FFT at the PCO–YSZ interface shown in Figure 2b support this conclusion; this

doubling is typical of the interface. Sheth *et al.*<sup>20</sup> observed similar defects in PCO films grown by PLD on YSZ; those authors attributed such image contrast features to threading dislocations. While our microstructure is consistent with those authors’ results, the region at the PCO–YSZ interface at room temperature was, in general, too disordered in our own images of sample A to resolve specific dislocation cores or Burgers vectors. However, the film lattice was otherwise possible to resolve with atomic resolution, as exemplified by the ADF-STEM image in Figure 2c.

Figure 2c also denotes the notation we use throughout to indicate sample orientation: “ $x$ -component” corresponds to the direction parallel to the film–substrate interface, along which PCO displacement is constrained by the substrate, and “ $y$ -component” refers to the direction normal to the film–substrate interface and unconstrained in displacement toward the film free surface. We also note here that there existed a layer of atomic disorder ( $\sim 10$  nm) at the film free surface in sample A. Figure 2a denotes that region by a dashed line, and our FFT and EELS analysis indicated a larger proportion of reduced cations and larger lattice volume in that region relative to the rest of the film. Those features were indicative of significant film reduction and associated chemical expansion in that area, and thus we attributed the features of that region to damage during sample preparation by focused ion beam (FIB) milling (see Experimental Section).

We quantified the as-prepared lattice spacing in the PCO film as a function of distance from the interface relative to the lattice spacing in the YSZ substrate within 10 nm of the interface, as shown in Figure 2d. Near the interface, strain in the PCO normal to the interface ( $y$ -component) was significantly larger than that parallel to the interface ( $x$ -component). This difference decreased with increasing distance from the interface and was approximately equal at a distance of  $\sim 40$  nm. This result is expected in that YSZ exhibits a smaller lattice parameter than PCO, such that the PCO  $x$ -component lattice parameter near the film–substrate interface is smaller than that of unconstrained bulk PCO. The PCO film strained normal to the interface under this constraint, and this anisotropic lattice distortion was reduced with increasing distance from the interface. We report this PCO lattice parameter change as a ratio with respect to the YSZ lattice parameter because the  $\sim 6\%$  lattice mismatch between these materials is well-established, this method allows us to account for image distortion due to tilt in the TEM under different imaging conditions, and because the YSZ lattice parameter at room

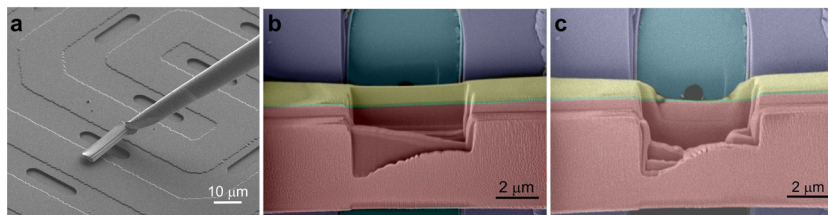


**Figure 3.** Scanning electron microscope image of a  $\text{Pr}_{0.1}\text{Ce}_{0.9}\text{O}_{2-\delta}$  (PCO) on yttria-stabilized zirconia (YSZ) cross section prepared by focused ion beam (FIB) milling. (a) After milling, sample B was placed on a high-temperature heating chip that uses Pt heating elements (spirals) to raise the sample temperature to  $650\text{ }^{\circ}\text{C}$ . (b) Higher-magnification image with false color shows the different regions of the FIB cross-section placed over a slit in the  $\text{Si}_3\text{N}_4$  of the heating chip. Colors indicate: YSZ substrate (pink), PCO film (green), Pt capping layer (yellow),  $\text{Si}_3\text{N}_4$  window (turquoise) and thicker  $\text{Si}_3\text{N}_4$  (purple). (c) Same area as in (b), but after a second FIB milling step to further thin the cross section and remove the majority of the Pt surface capping layer. This resulted in the interface region being suspended across the open window area of the thin  $\text{Si}_3\text{N}_4$  membrane.

temperature is a useful reference length in our subsequent experiments that incurred thermal expansion in both the film and substrate lattices but chemical expansion in only the PCO film lattice. We note here that the as-grown PCO film exhibited relatively invariant composition as a function of distance from the interface, as quantified by EELS. Except for the FIB-damaged region at the film free surface (*i.e.*, maximum distance in  $y$ -direction from the interface), neither the cation oxidation state nor the dopant distribution varied significantly throughout the film or near the linear defects. This result is also consistent with the room temperature results of Sheth *et al.*<sup>20</sup>

**Thermochemical Strain Anisotropy.** Having established the as-prepared PCO film structure, we next characterized film response upon a change in temperature or oxidation state. Using the spatial and chemical resolution afforded by STEM imaging coupled to EELS analysis, we imaged a cross section loaded on a high-temperature TEM holder at four conditions of temperature and oxidation state (see [Experimental Section](#) and [Figure 3](#)). Oxygen exchange in PCO begins above 500 °C, with the exchange rate increasing at higher temperatures. Therefore, to oxidize or reduce PCO samples, we held them at 650 °C using the *in situ* heating holder in oxidizing (air outside the TEM) or reducing (inside TEM vacuum of  $<10^{-11}$  atm) environments for at least 30 min prior to imaging. We estimated that the PCO film cross section of  $<100$  nm thickness would achieve equilibrium with such environmental conditions well within this time frame. To minimize oxygen loss upon re-entry into the TEM vacuum for imaging, we cooled our oxidized samples rapidly to room temperature, preventing further gas exchange. We note here that the YSZ substrate is not active to oxygen exchange, and so we do not expect significant changes in the YSZ oxygen content or associated lattice volume (beyond thermal expansion effects) due to those changes in environmental conditions.

[Figure 4](#) shows the lattice spacings of PCO and YSZ measured at these conditions parallel to ( $x$ ) and normal to ( $y$ ) the interface. [Figure 4](#) also shows the ratio of PCO lattice spacing normalized against the corresponding values for the YSZ substrate located within 15 nm of the PCO–YSZ interface, where we determined the interface position based on image contrast associated with defects at the interface discussed in the following section. We note that because we conducted high-temperature imaging on a different specimen than the specimen analyzed at room temperature in [Figure 2](#), with a different FIB cut orientation and imaging conditions, the lattice spacings observed for sample A in [Figure 2b](#) are not identical to those observed in [Figure 4a,b](#). Both the PCO and YSZ crystals exhibited thermal expansion; however, the PCO film also exhibited chemical expansion. This additional capacity of the PCO film to exhibit expansion due to cation valence and oxygen vacancy concentrations that vary with temperature can be recognized through comparison of the “reduced” and “oxidized” lattice spacing ratios. Note that PCO at temperatures  $>500$  °C is capable of fast oxygen exchange and is expected to equilibrate to the vacuum (low  $pO_2$ ) in the TEM column within minutes by releasing oxygen (*i.e.*, undergoing electrochemical reduction).<sup>35,43</sup> Thus, at 650 °C, PCO was reduced significantly within the 15–20 min required to focus the electron probe. However, at a lower temperature of 300 °C, comparison of preoxidized and prerduced samples was possible, allowing direct observation of thermal and chemical expansion.

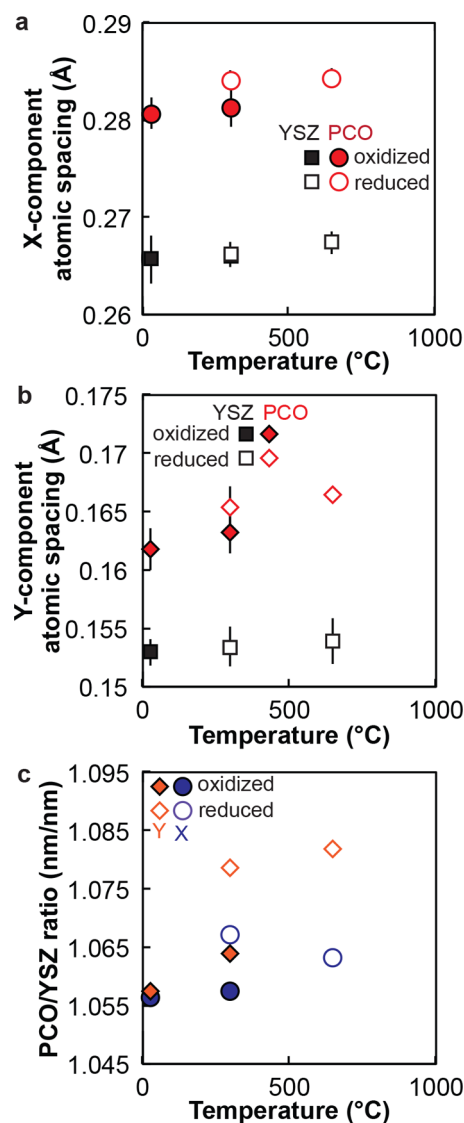


**Figure 4.** (a) Lattice spacing parallel to the interface ( $x$ -component) and (b) normal to the interface ( $y$ -component) in  $Pr_xCe_{1-x}O_{2-\delta}$  (PCO) and yttria-stabilized zirconia (YSZ) lattices at four conditions of temperature and oxidation state imaged by scanning transmission electron microscopy. We conducted sample imaging for the electrochemically reduced state of PCO (300 °C followed by 650 °C), followed by reoxidation of PCO and imaging (25 °C followed by 300 °C). We normalized PCO lattice spacing normal to the interface ( $y$ -component) with respect to the expected YSZ lattice spacing resulting from thermal expansion to account for varying tilt angles during different imaging sessions. We determined the  $y$ -component lattice spacing from the out-of-plane diffraction spots produced by the hexagonal FFT diffraction patterns from the STEM images. This hexagonal FFT pattern also means that the  $x$ - and  $y$ -component lattice spacings differ in magnitude. PCO lattice spacings reported as mean and standard deviation measured at multiple locations within 10 nm of the interface. (c) Ratios of PCO lattice spacing normalized by YSZ lattice spacing in the same conditions.

The EELS spectra in [Figure 5](#) confirmed the electrochemical reduction of PCO at elevated temperature. We recorded these spectra at a distance of 10 nm from the interface at each condition. The spectra shown in [Figure 5](#) exemplify the features used to characterize cation composition and oxidation state. The key features in these images are the Ce M5/M4 peak area

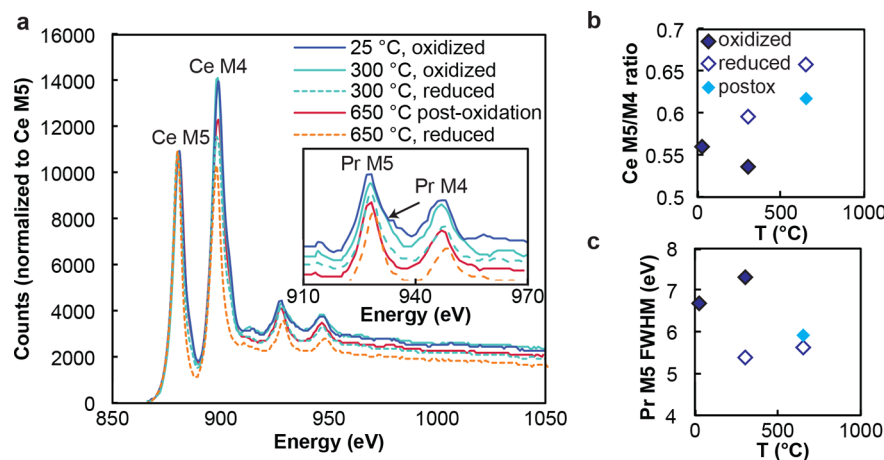


**Figure 5.** (a) Electron energy loss spectra at several imaging conditions of temperature and oxidation state. These spectra were shifted against the Ce satellite peak at 1163 eV which is not necessarily an immovable reference, and were collected at a distance of 10 nm from the yttria stabilized zirconia interface. Inset shows Pr M5 and M4 peaks after separate Pr background subtraction. (b) Increased Ce M5/M4 peak area ratio with increased temperature or prior sample reduction indicative of increased  $\text{Ce}^{3+}$  concentration. Additionally, the Pr M5 peak (highlighted by the black arrow) narrowed with Pr cation reduction. (c) Full width at half-maximum of the Pr M5 peak decreased as Pr reduced.

ratio (quantified in Figure 5b) and the shape of the Pr M5 peak; the EELS signature of PCO at different oxidation states was characterized previously and reported elsewhere.<sup>41,44</sup> Pr reduces preferentially to Ce, and when this occurs, the Pr M5 peak narrows and shifts to lower energy. This shape change was apparent for the reduced spectra in Figure 5, including the “post-oxidized” spectrum that we recorded upon heating the oxidized sample to 650 °C. We quantified the change in peak shape using the peak full width half-maximum reported in Figure 5c. The Pr M5 peak width did not change appreciably when we heated the reduced sample from 300 to 650 °C. In contrast, the peak narrowed with increased temperature (from 300 to 650 °C) for the oxidized sample. Elevated temperature of 650 °C should be sufficient to elicit oxygen loss (sample reduction) inside the TEM column. Thus, Pr contained in reduced samples or in samples above the oxygen exchange threshold temperature of  $\sim 500$  °C should be assumed to be chiefly in the +3 state.

The EELS signature for Ce oxidation state, as characterized by a change in the relative heights of the Ce M5 and M4 peaks (and associated areas) can be readily observed in Figure 5. For Ce, increased M5/M4 ratio and associated left-shifted M5 and M4 peaks (with appropriate peak referencing) indicate  $\text{Ce}^{4+} \rightarrow \text{Ce}^{3+}$  cation reduction.<sup>44</sup> Thus, it is clear that the “reduced” samples in Figure 4 were reduced to the point of Ce reduction, an effect that was most pronounced for sample reduction at 650 °C (orange, dashed line, Figure 5). Changes in the EELS signature for Pr reduction were quantifiable but less pronounced than those of Ce oxidation. We further note that the “post-oxidized” sample at 650 °C did not achieve complete reduction; this suggests that inside the TEM chamber the process of oxygen loss associated with Ce reduction was relatively slow (on the scale of 10–30 min) despite the small sample thickness (<100 nm). Note that we did not ascribe physical interpretation to the apparent peak shifts in Figure 5, as no standard peaks were available to calibrate spectra recorded at different times and under distinct *in situ* conditions.

Figure 4c illustrates that the strain variation with distance from the film–substrate interface that we observed in the as-grown film at room temperature (Figure 2d, sample A) was

absent upon reoxidation of PCO at high temperature (sample B). As described in the Experimental Section, sample B was subjected to elevated temperatures of up to 650 °C for extended times, in effect annealing the sample prior to high-temperature STEM imaging. This contrast in the magnitude of strain within 10 nm of the film–substrate interface in the as-prepared and postannealed specimens at room temperature suggests that the annealing process relieved interfacial stress sufficiently to relax the film lattice upon reoxidation at elevated temperature. If we refer to the distinct PCO lattice spacing in the *x*- and *y*-directions as “strain anisotropy”, then Figure 4 shows that such strain anisotropy was evident for all conditions except PCO oxidized at room temperature. Thermal expansion in PCO and YSZ was comparable (about 30% larger for PCO<sup>45,46</sup>) such that PCO lattice strain (relative to YSZ) parallel to the interface changed minimally under conditions allowing only thermal expansion. Even so, PCO expansion normal to the interface (*y*-component) increased slightly with increased temperature for the oxidized or reduced cases. In contrast, chemical expansion affected strain both along and normal to the interface (both *x*- and *y*-components) though strain normal to the interface was modulated more strongly. At 300 °C, PCO in the reduced state exhibited out-of-plane strain (strain in the *y*-direction) of 1.4% as referenced to the oxidized state, whereas in-plane strain along the interface (strain in the *x*-direction) was only 0.9% upon reduction. We estimate the measurement error for strain along the interface as  $\pm 0.15\%$ , given that this in-plane strain was 0.6% for PCO reduced at 650 °C. Even with this level of measurement uncertainty, the strain normal to the interface was  $\sim 50\%$  greater than that parallel to the interface, indicating clearly that chemical expansion resulted chiefly in increased atomic spacing normal to the interface (and therefore increased film thickness) due to the film–substrate interface constraint. As measurable expansion was also quantified parallel to the interface, we assert that the chemical expansion coefficient can be understood to be both *thickness-dependent* and *spatially anisotropic* with respect to distance from the interface.

By considering Figure 4 and the chemical expansion coefficient of PCO, we can infer differences in point defect

concentration, as quantified by the change in nonstoichiometric parameter  $\Delta\delta$  that existed in the PCO films in the oxidized and reduced states *in situ*. Using the strain parallel to the film–substrate interface resulting from reduction of PCO at 300 °C,  $\Delta\delta$  is approximately 0.1 according to eq 2. Taking account of the strain measured for the reduced sample at 650 °C, this estimate of  $\Delta\delta$  is 0.06–0.1. Assuming that mechanical constraint of the substrate amplified the film strain normal to the interface (*y*-component) by approximately a factor of 2,<sup>20</sup> we can also estimate  $\Delta\delta$  independently at 0.08. Since we observed measurable and repeatable strain parallel to the film–substrate interface, a slightly larger value of  $\Delta\delta$  of about 0.1 appears plausible. Given that these films have a Pr concentration of  $x = 0.1$ , the reduction of Pr can contribute a change in  $\delta$  of only 0.05. Therefore, the remaining strain must be attributed to that arising from Ce reduction, an assertion that is further supported by our EELS data in Figure 5. Given these results, we infer that either the effective partial pressure of oxygen  $p_{\text{O}_2}$  within the TEM chamber was  $<10^{-18}$  atm (the point of Ce reduction in PCO at 650 °C<sup>14,47</sup>), and/or the reduced PCO film cross section was significantly more reduced than expected based on available defect models. Since the TEM vacuum was at about  $10^{-11}$  atm for the results reported herein, a reducing gaseous species such as H<sub>2</sub> or CO would need to have been present to achieve such a low  $p_{\text{O}_2}$ , which seems unlikely. The electron beam dosage may have induced some reduction of PCO, but we intentionally varied the imaging location to minimize such effects, and similar beam dosages applied to oxidized samples did not cause detectable Pr or Ce reduction (see Figure 5). Therefore, we attribute the observed lattice expansion to a combination of low  $p_{\text{O}_2}$  ( $<10^{-12}$  atm) and enhanced sample reduction in these very thin ( $<100$  nm) PCO cross sections.

**Interface Structure.** The variation of chemical expansion exhibited by the PCO films as a function of orientation with respect to the film–substrate interface results from the mechanical constraint of the interface. We conducted an annealing study of the PCO–YSZ interface upon initial heating to 650 °C inside of the TEM (sample B; see Experimental Section and Figure S8). Figure 6 shows that periodic image contrast features existed normal to and near (if not transecting) the interface during this initial heating study, with a spacing of  $\lambda \sim 4$  nm. These features resulted from lattice distortion around misfit dislocations that caused diffraction-based contrast variation in the image in the region of disorder. During sample annealing, the sample lattice resolved more clearly, and inclusions with dissimilar orientation realigned with the rest of the PCO lattice.

When we subsequently imaged the same sample by STEM, the interface continued to exhibit a periodic array of defects, as shown in Figure 7a,c. Geometric phase analysis of these images produced strain maps such as those shown in Figure 7b,d, indicating periodic hourglass-shaped strain features along the interface with a characteristic spacing of  $\sim 4$  nm. This spacing agrees well with that of  $\lambda$  identified for the series of images included in Figure 6, and the strain profiles in the GPA images are consistent with GPA contrast expected of edge dislocations. High-resolution imaging of these interfacial defects (Figure 7e) also indicated a mismatched lattice at this interface, and inverse Fourier transform analysis resolved the position of an apparent extra lattice half-plane (Figure 7f, arrow).

Several previous TEM studies have reported observation of edge dislocations at the interface between epitaxial ceria (both

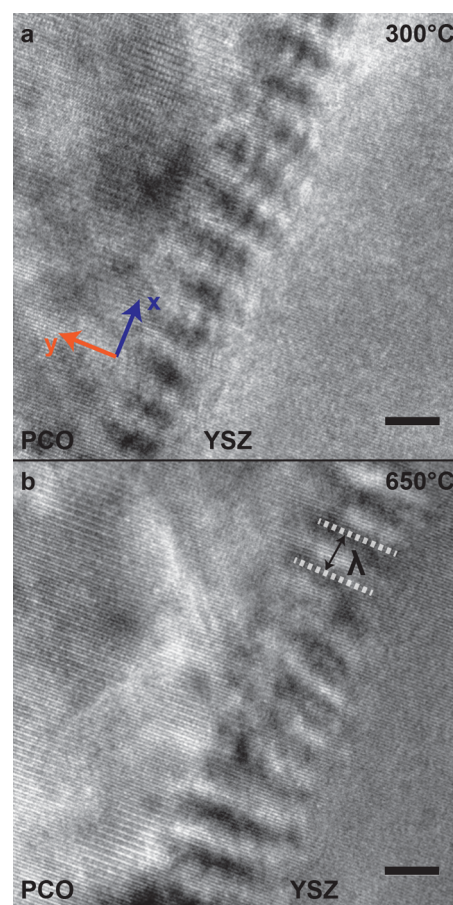


**Figure 6.** Phase contrast transmission electron microscope images at the same resolution of the PCO–YSZ interface at (a) 300 °C and (b) 650 °C and at different locations showed interfacial contrast fringes. Interfringe spacing  $\lambda$  marked in (b) is  $\sim 4$  nm, agreeing well with edge dislocation spacing determined based on scanning transmission electron microscopy images. Further analysis of interfacial contrast is available in Supporting Information. Scale bars are 5 nm.

undoped and Sm-doped) and YSZ substrates.<sup>24,36,37</sup> Generally imaged at room temperature, these dislocations were present in both oxidized and highly reduced films for which sample reduction (even to an ordered structure with  $\delta = 0.3$ ) was induced by high energy irradiation with the electron beam.<sup>20,24,36</sup> The spacing of CeO<sub>2</sub>–YSZ misfit dislocations reported previously for the (100) orientation ranges from 3.7 to 4.8 nm and is understood generally to relieve misfit stress at the interface.<sup>20,36,37</sup> In molecular dynamics simulations of CeO<sub>2</sub> recrystallization from an amorphous phase adjacent to crystalline YSZ, arrays of misfit edge dislocations appeared spontaneously, along with other mixed screw-edge dislocations that extended into the film.<sup>48</sup> Sheth *et al.* also observed by TEM the existence of threading dislocations for PCO films grown on YSZ.<sup>20</sup>

Periodic contrast fringes similar to those in Figure 6 have been observed by TEM in interfaces such as heteroepitaxial GaSb/GaAs and grain boundaries in Bi<sub>0.5</sub>Sb<sub>1.5</sub>Te<sub>3</sub>.<sup>49–51</sup> In prior work, those features were attributed by the authors as resulting from periodic arrays of misfit dislocations. In our own images, the disordered nature of the lattice in this interfacial region precluded direct, lattice-resolved observation of these features during the initial annealing cycle, although later analysis *via*

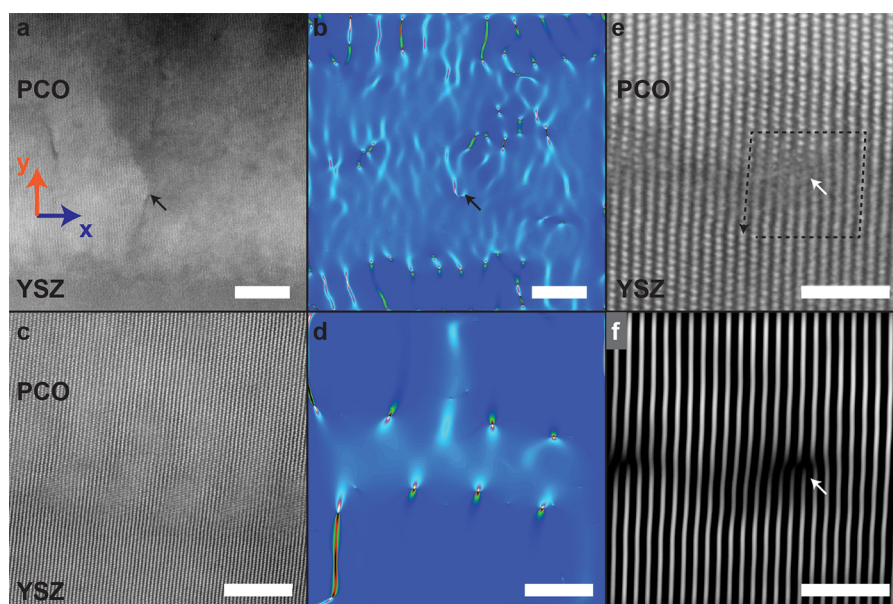


**Figure 7.** (a) Scanning transmission electron microscope image of preoxidized  $\text{Pr}_x\text{Ce}_{1-x}\text{O}_{2-\delta}$ -YSZ interface with a threading defect at room temperature. (b) Geometric phase analysis of (a) showing interfacial periodic strain field and threading linear defect (indicated by black arrow). Scale bars for (a) and (b) are 10 nm. (c) ADF-STEM image of fully reduced PCO-YSZ interface at 300 °C and (d) corresponding geometric phase analysis. The distance between strain-field cores is 4.1 and 4.3 nm in (b) and (d), respectively. Scale bars for (c) and (d) are 5 nm. (e) High-resolution image of a misfit dislocation at the PCO-YSZ interface at room temperature with Burgers circuit drawn (black, dashed line); (f) ADF-STEM image from (e) after applying a positive mask filter to the FFT to select only one set of reflections to highlight the dislocation location (white arrow). The distance between dislocation cores in this image is 4.3 nm. Scale bars for (e) and (f) are 2 nm.

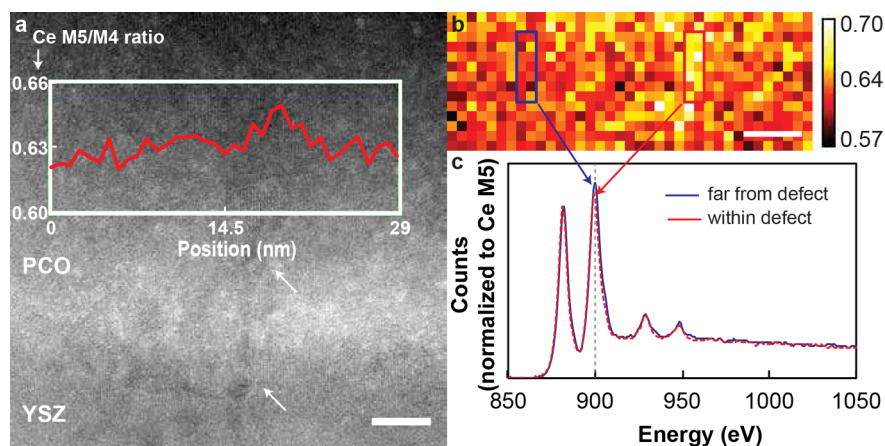


**Figure 8.** (a) ADF-STEM image of a linear defect (white arrows) propagating from the PCO-YSZ interface through the PCO film at 650 °C toward the PCO free surface with selection region for EELS data collection highlighted. The plot shows the average Ce M5/M4 ratio moving left to right across selection region, showing a maximum at the linear defect. (b) Map of the Ce M5/M4 EELS peak area ratio from the highlighted region in (a). (c) Comparison of EELS spectra within and outside the linear defect confirmed Ce reduction inside the defect through both changing peak height and peak shift. Scale bars are 5 nm.

STEM showed stress and lattice features consistent with edge dislocations with comparable interfringe periodic spacing  $\lambda$ . Upon considering and eliminating other possible sources of periodic contrast at the interface (see discussion of Figures S1–S4 in Supporting Information, SI), we conclude that the periodic contrast and the periodic line defects observed by TEM and STEM, respectively, were both due to misfit dislocations and associated strain fields. We also note that during sample annealing, both the interfringe periodic spacing  $\lambda$  and the width of these contrast features evolved as a function of temperature, pointing to possible stress relief during chemical expansion at the highest temperatures. Further discussion of those observations can be found in the SI (Figures S1–S4).

After this annealing process, we also imaged and analyzed the PCO-YSZ interface *via* STEM with EELS to consider measurable features of space charge and cation segregation at the interface. We observed no evidence of cation segregation, and, although expected based on previous observations of epitaxial  $\text{CeO}_2$ -YSZ interfaces,<sup>24</sup> we found limited evidence of space charge in our own samples. For the oxidized film at 300 °C, we resolved an apparent increase in the  $\text{Pr}^{3+}$  concentration at the PCO-YSZ interface, possibly indicating space charge. However, we identified no such trend for  $\text{Ce}^{3+}$  in highly reduced samples. Supporting Figure S5 provides the EELS spectra for this result, along with additional discussion in SI.

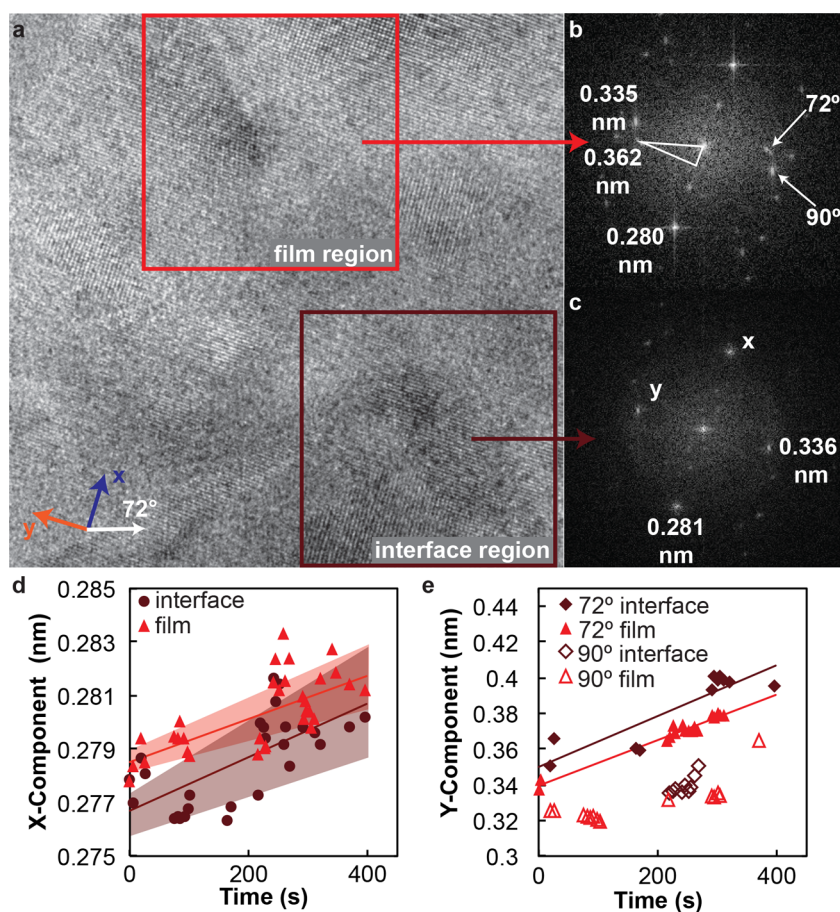


**Figure 9.** (a) Example TEM image from time series collected during sample reduction *in situ*, showing regions selected near and far from the PCO–YSZ interface for lattice spacing analysis. (b) FFT resulting from the film region with the 72° and 90° *y*-component (normal to the interface) lattice reflections highlighted by white arrows. (c) FFT from the interface region in (a). (d) Measured *x*-component (parallel to the interface, with shaded 95% confidence intervals for the linear fit) and (e) *y*-component lattice spacing vs time as the cross section equilibrated with the TEM vacuum (*i.e.*, reduced).

Taken together, we conclude that the PCO films grown on YSZ exhibited periodic arrays of dislocations that exerted strain fields identifiable from both TEM and STEM images. At sufficiently high temperatures and at chemical-expansion induced stresses, these defects appeared mobile enough to partially relieve interfacial stress, as discussed further in SI. Upon sample cooling and reoxidation, those defect features remained immobile in position and some Pr<sup>3+</sup> enrichment appeared at the PCO–YSZ interface accompanied by emergence of longer range, threading defects.

**Threading Defects.** After sample reoxidation (see Experimental Section and SI Figure S8 for flowchart of experimental procedures), we observed by ADF-STEM defects extending from the film–substrate interface that were not visible previously. Figures 7 and 8 show one such defect, along with an EELS map of the associated Ce M5/M4 peak area ratio. The EELS map exhibited a maximum at the position of the linear defect, shown also in the inset to Figure 8a. Figure 8c compares spectra within and far from the defect. We detected this signature, which indicates increased sample reduction at the position of the defect, to a lesser degree for the same defect at room temperature (SI Figure S6) and also for a similar defect imaged for the oxidized sample at 300 °C (SI Figure S7). We consistently observed sample reduction relative to the lattice at these defects, both at low-temperature oxidized conditions (when the rest of the sample should contain minimal Pr<sup>3+</sup> or

Ce<sup>3+</sup> content) and at high-temperature reduced conditions. This localized reduction implies that these defects acted as traps for reduced cations and/or oxygen vacancies relative to the rest of the lattice, establishing spatial heterogeneity of such defects within the lattice.

Linear defects that appeared in reoxidized (redox cycled) samples thus may have acted as sinks for Ce<sup>3+</sup> cations and possibly also for corresponding oxygen vacancies. Because the cation oxidation state change requires only small polaron hopping, oxygen vacancy diffusion (and associated volume change) could be a mechanism of stress relief during reoxidation at 650 °C. Not only should reduced cations correlate with increased sample volume (which is difficult to resolve given the disordered nature of these regions), but they would also potentially affect charge transport and gas reactivity properties.<sup>42,52</sup> For example, Sun *et al.* determined that edge dislocations in CeO<sub>2</sub> could cause charged defect localization of both reduced cations and oxygen vacancies within the tensile and compressive strain fields around the dislocation. The association between these charged defects could then trap further ion motion, potentially impeding oxide ion conductivity.<sup>42</sup> While the exact classification of the defects imaged in Figures 8, S6, and S7 could not be identified, the general result of Sun *et al.* is likely still applicable. This threading defect, which trapped an enriched concentration of reduced cations, would likely also act as a barrier to oxygen vacancy diffusion.

While the relatively degraded lattice resolution within the defect precluded measurement of lattice spacing, such image quality in that region also suggested a high degree of disorder such as might be expected from a relatively large concentration of oxygen vacancies. It is also possible that this was actually a space-charge region, in which case a large concentration of reduced cations surrounding an oxygen-vacancy-enriched core should correspond to increased lattice parameter.<sup>17,23</sup>

Appearance of such defects in redox cycled, mechanically constrained films could explain several observed differences between film and bulk PCO *in situ*, including enhanced oxygen vacancy concentrations,<sup>35</sup> relatively lower elastic modulus than expected for defect models of bulk PCO, and a high degree of variability in the measured Young's modulus by nano-indentation.<sup>16</sup> Space-charge regions of reduced cations distributed inhomogeneously throughout a film would be expected to have larger volume than the surrounding lattice, causing associated, inhomogeneous decreases in elastic modulus. Furthermore, there is the potential that propagation of such defects to the film free surface could catalyze oxygen vacancy formation, even as it could impede charge transport.<sup>42,52</sup> These defects appeared in our samples after reoxidation that corresponded to a change in stress state (in the tensile direction); if this is a general effect in other nonstoichiometric oxides, this mechanism could also mediate effects of tensile strain on oxygen exchange reactivity and diffusivity.

**Dynamic Imaging of *In Situ* Oxygen Breathing.** We conclude our discussion with direct observation of PCO expanding during *in situ* re-reduction at 650 °C. After oxidizing the PCO film outside the TEM column, we inserted the sample into the microscope and recorded images as PCO equilibrated by releasing oxygen into the TEM vacuum (see [Experimental Section](#) and [Figure S8](#)). While others reduced CeO<sub>2</sub> *in situ* by electron-beam irradiation previously,<sup>36,53</sup> those studies did not analyze in detail the anisotropic or localized chemical expansion during the reoxidation process. After focusing on a fully oxidized film at room temperature and 200 °C, we rapidly heated the film (within 2 min) to 650 °C inside the TEM column. We then collected a time series of phase-contrast high resolution TEM images such as the one shown in [Figure 9a](#) while the sample reduced (and underwent chemical expansion) inside the TEM vacuum. We collected images of many regions in the PCO film in order to prevent any sample reduction *in situ* by the electron beam. As shown in [Figure 9](#), for each image we analyzed two regions: one adjacent to the interface and one far (>20 nm) from the interface. These images exhibited two characteristic types of FFT: a hexagonal (72°, [Figure 9b](#)) pattern and a rectangular (90°, [Figure 9c](#)) pattern. These patterns sometimes coexisted within an analyzed image, indicating slightly different lattice projections as dominant features in different parts of the film during rereduction. We observed no such lattice variability in the previously discussed STEM images for either oxidized or reduced samples, suggesting that the redox process may have involved some local nucleation phenomena or lattice distortion. It is also possible that these small grains nucleated near and were constrained by residual amorphous surface layers of the TEM cross section during annealing.

We reported the lattice spacing both parallel to the interface ( $x$ ) and normal to the interface ( $y$ ) based on the FFT patterns as a function of time in [Figure 9d,e](#). Both data sets showed a positive slope with time, reflecting lattice dilation as the sample

actively released oxygen from its structure. We were able to resolve the  $x$ -component lattice planes more easily than the  $y$ -component planes and also more consistently between the two lattice projections. This enabled a statistical analysis of the linear fits applied to the  $x$ -component data. This analysis produced 95% confidence intervals (CI) for the intercept and slope of the linear fit ([Figure 9](#) shaded regions), from which we determined that the mean PCO lattice spacing along the direction parallel to the interface ( $x$ ) was smaller near the interface (0.277 nm) as compared to that located more than 20 nm from the interface (0.279 nm). We did not find the differences in slope to be statistically significant, in that the 95% CIs for the slopes of the linear fits overlapped. However, these data are consistent with the concept that the region nearest the interface existed in a state of compression relative to the bulk, prior to chemical expansion. We further found that this relative (though statistically insignificant) difference in  $x$ -component lattice parameter near and far from the interface was also retained during film expansion.

The PCO film also exhibited positive strain with time in the direction normal to the interface, which was larger for the region closest to the interface. The overall apparent slope of this lattice strain direction with time was statistically larger than that observed for the strain parallel to the interface, indicating (consistent with [Figure 4c](#)) that chemical expansion was more pronounced in the direction normal to interface ( $y$ ) than parallel to the interface ( $x$ ). However, we note that the  $y$ -component data in [Figure 9e](#) are too sparse, with too large of an uncertainty range, to identify statistical differences between the interface and film regions for the intercepts or slopes. This spatially inhomogeneous strain also could not be attributed unambiguously to phase separation or ordering (see [SI](#)). The time series images therefore demonstrated the PCO exhibiting spatially anisotropic chemical expansion *in situ* as the structure breathed oxygen out of the lattice.

## CONCLUSIONS

We reported *in situ* TEM, STEM, and EELS analysis of chemical expansion in the model nonstoichiometric oxide thin film Pr<sub>0.1</sub>Ce<sub>0.9</sub>O<sub>2- $\delta$</sub>  grown on YSZ substrates. We found that such PCO films exhibited anisotropic chemical expansion that was more pronounced in the direction normal to the interface ( $y$ -component) relative to the direction parallel to the film–substrate interface ( $x$ -component). This lattice expansion also varied with distance from the interface: local strain parallel to the interface was smaller near to the interface, and the reverse was true for strain normal to the interface. PCO films exhibited periodic arrays of strain fields imaged by ADF-STEM, consistent with misfit dislocation features, that changed size during thermochemical expansion. Upon sample reoxidation, threading defects appeared in the PCO cross sections. These defects trapped reduced cations for both oxidized, low-temperature conditions and reduced, high-temperature conditions, possibly impeding charge transport or affecting local oxygen vacancy formation energies. Finally, we directly observed the PCO film undergoing chemical expansion as it released oxygen, dynamically imaging this anisotropic, position-dependent chemical expansion *in situ*.

These results demonstrated several mechanisms facilitating chemical expansion in thin film nonstoichiometric oxides, including strain anisotropy, long-range defect formation, and spatially inhomogeneous strain and composition. Films can be expected to exhibit significant strain normal to the film–

substrate interface that may be enhanced for structures that are also thin in the orthogonal dimension, such as the cross sections considered in this study. The observed anisotropic chemical expansion and lattice strain showed that interfacial stress persists *in situ*. This direction-dependent chemical strain could also impact chemomechanically coupled, volume-averaged properties such as elastic moduli or oxide ion diffusivity. Furthermore, threading defects that appear during redox cycling may localize charged cations *in situ*, potentially impacting total oxygen vacancy content, lattice stiffness, and transport properties. These results provide a direct and detailed analysis of chemical expansion in a thin film nonstoichiometric oxide that will inform the design of high-temperature oxide actuators or strain-engineered functional oxides for applications involving gas exchange, storage, or ionic conductivity.

## EXPERIMENTAL SECTION

**Sample Preparation.**  $\text{Pr}_{0.1}\text{Ce}_{0.9}\text{O}_{2-\delta}$  films were prepared by pulsed laser deposition from oxide targets. The films were deposited onto (001)-oriented single crystal YSZ (8 mol % of  $\text{Y}_2\text{O}_3$ -stabilized zirconia) substrates ( $10 \times 10 \times 0.5 \text{ mm}^3$ ; MTI Corporation, Richmond, CA). The 2.5 cm diameter oxide target was fabricated from PCO powders prepared through a Pechini-based gel process described briefly below.<sup>34</sup> The following starting materials were utilized: cerium(III) nitrate hexahydrate, 99.99% (Sigma-Aldrich), praseodymium(III) nitrate hydrate, 99.9%, ethylene glycol (Alfa Aesar), and anhydrous citric acid (Fisher Scientific). Citric acid and ethylene glycol were mixed with aqueous solutions of  $\text{Ce}(\text{NO}_3)_3$  and  $\text{Pr}(\text{NO}_3)_3$  at 80 °C until polyesterification resulted in the formation of a gel. After being dried in an oven at 110 °C, the as-obtained powder was fired at 450 °C for 4 h and then at 700 °C for 3 h in flowing air. The PCO powders were examined by X-ray diffraction (Rigaku H3R Cu source powder diffractometer) and were found to have a single phase fluorite structure. Dense PLD targets were then prepared by isostatic pressing of PCO powder followed by sintering at >1400 °C.

The PLD system (Neocera Inc., Beltsville, MD) was operated with a KrF excimer laser (Coherent COMPex Pro 205) emitting at 248 nm, with 400 mJ/pulse and repetition rate of 8 Hz. The substrates were heated to 600 °C during deposition, while the oxygen pressure was maintained at 10 mTorr after pumping the background pressure to less than  $8.56 \times 10^{-6}$  Torr. The film was deposited with 45000 shots after 2000 preablation shots with a substrate to target distance set to 7 cm. Following deposition and prior to cooling, the oxygen pressure in the chamber was increased to approximately 6–7 Torr to facilitate complete oxidation of the film. Film thickness was determined to be 196 nm *via* surface profilometry (KLA-Tencor P-16+ stylus profiler) of the film deposition edge.

Two PCO–YSZ cross-sectional test specimens with a final cross-section thickness of 50–100 nm were prepared by FIB milling using a Zeiss Crossbeam 540 instrument fitted with an Omniprobe 400 micromanipulator. Samples were transferred from a bulk specimen to windowed test points on a DENS chip. A thin layer of Pt was deposited over the target area using the electron beam (2 nA beam current at 5 kV for approximately 60 s) prior to any ion beam exposure. After this, a standard *in situ* procedure was adopted for liftout.<sup>55</sup> Initial setup began with a deposition of Pt measuring  $20 \times 2 \times 1.5 \mu\text{m}$  using the  $\text{Ga}^+$  ion beam, followed by coarse milling steps using a 30 kV/30 nA beam to remove the bulk of material. The sample was further thinned to a thickness of  $\sim 1.5 \mu\text{m}$  using a beam current of 30 kV/1.5 nA and then undercut in preparation for release and lifting out. Throughout the text, samples imaged at room temperature and at elevated temperature are referred to as samples A and B, respectively.

Liftout was carried out by welding the specimen to an Omniprobe needle using Pt, released with a FIB cut, and then lifted out with the stage at 0° tilt. Once clear of the bulk material, the micromanipulator needle was rotated by 90° to present the specimen to the imaging chip. For sample B, this was in the geometry shown in the SEM image in Figure 3a. The sample was then secured on the chip with ion-beam-

deposited Pt. The chip was then reoriented for thinning of the lamella and, for high-temperature imaging, milling of a window into the nitride membrane. Further thinning was performed at 30 kV and 300 pA, until the Pt appeared transparent in an 8 kV SE image,<sup>56</sup> indicating a thickness of  $\sim 120 \text{ nm}$ . Final polishing was conducted at a reduced voltage of 2 kV to further thin and minimize the amount of damage and reduce levels of implanted Ga in the final specimen to final electron transparency at 5 kV electron energy.

Figure 3a–c shows sample B attached to a heating chip, including false coloring to denote different materials both before and after additional milling to extend the slit in the  $\text{Si}_3\text{N}_4$  for improved image resolution.

**Imaging and EELS.** Three microscopes were used to acquire images and spectroscopic analysis described below. Initial room temperature imaging of as-grown PCO films on YSZ (sample A) was conducted using an aberration corrected JEOL JEM-2200MCO field emission gun TEM/STEM operated at 200 keV, equipped with CEOS image/probe correctors. *In situ* imaging at high temperatures up to 650 °C was conducted using a commercially available *in situ* heating holder from DENS Solutions (SH30-4M-FS). The resistance of the platinum coil in the heating chip (DENS Solutions DENS-C-30) is monitored in a four-point configuration, and the temperature is calculated using the Callendar–Van Dusen equation (with calibration constants provided by the manufacturer). Slits were produced into the  $\text{Si}_3\text{N}_4$  membrane by FIB milling. Phase contrast transmission electron microscopy of samples at elevated temperatures was conducted with a standard JEM-2100 (JEOL) transmission electron microscope operated at 200 kV, with a  $\text{LaB}_6$  filament, while both high-temperature and room temperature annular dark-field scanning transmission electron microscopy (ADF-STEM) of sample B was conducted using a JEOL ARM-200F microscope operated at 200 kV, and equipped with an electron energy loss spectrometer.

Thermal and chemical expansions of the PCO film in sample B were induced, respectively, by controlling film temperature (using the DENS *in situ* heating chip) or changing the oxidation state of the PCO film by high-temperature annealing in either oxidizing (air) or reducing (TEM vacuum  $< 10^{-11}$  atm) environments. While both PCO and YSZ were expected to respond to changes in temperature with thermal expansion (increased lattice parameter with increased temperature), high-temperature annealing in oxidizing or reducing environments was only expected to induce chemical expansion in PCO because YSZ is not expected to be active to oxygen exchange. Because PCO undergoes oxygen exchange above 500 °C, it was also possible to trap PCO films in an oxidized or reduced state by rapidly cooling samples below the 500 °C threshold after annealing. For PCO, oxygen loss and associated cation reduction (caused by annealing at high temperature inside the TEM vacuum) should result in increased lattice parameter due to chemical expansion. The data presented in Figures 4–9 are the result of a series of experiments described below and presented in the form of a flowchart in Supporting Figure S8. Figure S8 also illustrates schematically how changes in control variables (*e.g.*, *T* or oxidation state) should change lattice parameters in PCO and YSZ, respectively.

An initial annealing study was conducted using the JEM-2100 while heating sample B from room temperature to a maximum temperature of 650 °C in increments of 50–100 °C and imaging along the film and interface cross section. This resulted in substantial electrochemical reduction of PCO while inside the TEM column at  $T > 500$  °C. The sample was rapidly cooled to room temperature to maintain this reduced state and then imaged and analyzed *via* EELS using the ARM-200F microscope at 300 and 650 °C. Sample B was then heated to 650 °C for 30 min outside of the TEM column to enable reoxidation of the PCO film. To observe sample reduction *in situ*, sample B was cooled rapidly to room temperature and heated to 200 °C with image focusing adjustments at each temperature, before rapidly heating the sample to 650 °C within 2 min inside the JEM2100. For the next 7 min, sample equilibration to the column vacuum was observed by continuous imaging along the film near the interface; images were recorded every 10–30 s, with the imaging location translated every 0.5–2 min. The sample was then reoxidized again at 650 °C in air and

placed in the ARM200 at room temperature. Imaging and EELS analysis were conducted at room temperature, followed by 300 °C (a temperature sufficient to prevent significant oxygen loss despite the TEM vacuum), followed by 650 °C. This last condition following intentional oxidation of the PCO is labeled “post-oxidation” or “postox” in the figures, to distinguish from image acquisition at 650 °C prior to forced oxidation. The sequence of experiments is illustrated in Supporting Figure S8, which also lists which figures draw data from which experiments.

EELS data were gathered using the ARM-200F microscope for an energy range of 300–2350 eV. To mitigate sample reduction by electron beam dosage, the imaging location was frequently adjusted for all imaging conditions. However, little evidence of beam-induced sample reduction was observed during imaging, due to the larger cross-section thickness compared to that in the reports of Sinclair *et al.*<sup>36</sup>

**Data Analysis.** Images were analyzed using Digital Micrograph version 3. To determine lattice spacing in PCO and YSZ, FFTs of TEM and STEM images were analyzed for peak positions using the Measure Spacings and Angles script in the DiffTools package available from D.R.G. Mitchell.<sup>57</sup>

Images above reference the  $x$ – $y$  plane as the imaged cross-section plane of the PCO lattice, with the image  $z$ -axis oriented along columns of atoms extending into the milled cross section. We thus refer to the displacements normal to the film–substrate interface as “out-of-plane” and select a  $y$ -axis orientation normal to the interface. Thus, displacements normal to the film–substrate interface are denoted as those extending in the  $y$ -direction normal to the interface or “out-of-plane” because such displacements would indeed represent film thickness increased or decreased in a direction perpendicular to the film plane and free surface of the film in plan view (*i.e.*, rotated 90° from the cross-sectional view of the TEM image plane). Displacements parallel to the interface are denoted as those observed in the  $x$ -direction, or “in-plane.” Clearly, the  $z$ -axis in this orthogonal axis set is normal to the cross-section surface, and any misorientation of the lattice displacements with respect to the  $x$ – $y$  axes refers to those offset from the film–substrate interface normal.

To determine the  $x$ - and  $y$ -components of PCO lattice spacing for ADF-STEM data at each condition, four to eight square regions of 10 × 10 nm were selected adjacent to the interface, and the FFT peak positions and angles were measured. Because FFT representations of the ADF-STEM images produced a hexagonal pattern as shown in Figure S9, the  $y$ -direction projection of the out-of-plane spots ( $\theta \sim 72^\circ$ ) were used to determine the “ $y$ -component” lattice spacing normal to the interface. The resulting magnitudes of  $x$ - and  $y$ -component spacing were averaged for each condition and compared to the spacings measured in the same imaging conditions for the YSZ substrate. In the case of rectangular lattice projections (sample A room temperature images and parts of sample B images used for Figure 9), this analysis did not require the additional step of accounting for angles  $\theta$ . Strain maps were produced by geometric phase analysis of  $x$ -component or in-plane strain parallel to the film–substrate interface, using the FRWRTools plugin for Digital Micrograph written by Koch.<sup>33</sup> The following parameters were used for GPA: 3 nm resolution, 1 nm smoothing.

Observed strains were computed with reference to the YSZ sample, specifically by determining the ratio of PCO lattice spacing to YSZ lattice spacing at the same imaging condition ( $T$ , oxidized or reduced sample) for each FFT peak of interest and then comparing the difference in this ratio between oxidized and reduced states. For example, to compute the chemical strain perpendicular to the interface at 300 °C for the reduced sample, the change in this ratio ( $[\text{PCO } y\text{-spacing}/\text{YSZ } y\text{-spacing in reduced state}] - [\text{PCO } y\text{-spacing}/\text{YSZ } y\text{-spacing in oxidized state}]$ ) was computed and then divided by the ratio in the oxidized case, which gave the chemical strain perpendicular to the interface. This calculation assumed, consistent with expectations, that only PCO, and not YSZ, responded to oxidation or reduction conditions at high temperature. The lattice spacing in the YSZ for each condition was determined based on FFT analysis of the maximum square of available YSZ lattice adjacent to the PCO–YSZ interface. The position of the interface was identified by image contrast

associated with defects at the interface as shown in Figure 7. Between two and six squares of YSZ lattice were analyzed for each condition, with average side length 11–13 nm for Figures 4 and 7 nm for Figure 2d. The choice to use YSZ as an internal reference length scale allowed control for image distortion due to tilt variation among different imaging conditions, while also providing a length scale robust to errors in the built-in scale bar of the TEM. Changes in defect chemistry based on observed strains were estimated by applying the chemical expansion coefficient of PCO ( $\alpha_c = 0.087$ ) and eq 2.<sup>6</sup>

To improve image signal-to-noise ratio, images from the annealing study were stitched together using the pairwise stitching toolbox in Fiji.<sup>58,59</sup> The width and periodic interfringe spacing for contrast fringes at the PCO–YSZ interface were analyzed using ImageJ, as described in SI and Figure S2.

EELS data were analyzed following the background subtraction procedure described by Bowman *et al.*<sup>41</sup> and briefly summarized here. Background subtraction for the Ce peaks was conducted by fitting an exponential loss function to a 50 eV window that was positioned to end 5 eV below the Ce M5 peak. For the Pr peaks, background subtraction was done by a two-window procedure available in Digital Micrograph version 2, with a 5 eV window below the Pr M5 peak and a second window from 1120 to 1165 eV; that window was well beyond the high energy loss tail of Pr. The Ce M5 and M4 peak areas were measured based on integrating 20 and 25 eV fitting windows after background subtraction, respectively, spaced by 1 eV and starting at ~871 eV. The Pr M5 and M4 peaks were similarly characterized starting at 920 eV, and the full width at half-maximum of the Pr M5 peak was determined after applying a double-Gaussian fit to the peak (after background subtraction) between 900 and 938 eV. This peak fitting was conducted using the curve-fitting toolbox in Matlab. The Cornell Spectrum Imager plugin for ImageJ was also used to handle, view, and compare EELS spectrum image files and maps.<sup>60,61</sup>

Time series data were fitted by linear regression. For the  $x$ -component lattice spacing, sufficient data density and range were available to apply a bootstrapping procedure to determine errors in fitting coefficients.<sup>62</sup> Using a custom Matlab code, the slope and intercept of the linear fit of  $x$ -component lattice spacing *versus* time was recomputed from 1000 resampled data sets to identify 95% confidence intervals for these parameters.

## ASSOCIATED CONTENT

### Supporting Information

The Supporting Information is available free of charge on the ACS Publications website at DOI: 10.1021/acsnano.7b07732.

Additional discussion and characterization of interfacial structure, threading defects, *in situ* breathing, analysis methods, and a flowchart of high-temperature experiments (PDF)

## AUTHOR INFORMATION

### Corresponding Authors

\*E-mail: jamie.warner@materials.ox.ac.uk.

\*E-mail: krystyn@mit.edu.

### ORCID

Jamie H. Warner: 0000-0002-1271-2019

Krystyn J. Van Vliet: 0000-0001-5735-0560

### Notes

The authors declare no competing financial interest.

## ACKNOWLEDGMENTS

The authors gratefully acknowledge support from the U.S. Department of Energy, Basic Energy Sciences, Division of Materials Science and Engineering under award number DE-SC0002633 (Chemomechanics of Far-From-Equilibrium Interfaces, Program Manager J. Vetrano). J.G.S. thanks the Hugh

Hampton Young Memorial Fund for fellowship support. J.H.W. thanks the support of the Royal Society and the EPSRC Grant Code EP/KO40375/1 for the South of England Analytical Electron Microscope. The authors thank H. Sawada for his assistance with TEM and EELS data collection, and B. Sheldon and S. Kumar for useful discussions.

## REFERENCES

- (1) Tuller, H. L.; Bishop, S. R. Point Defects in Oxides: Tailoring Materials Through Defect Engineering. *Annu. Rev. Mater. Res.* **2011**, *41*, 369–398.
- (2) Swallow, J. G.; Kim, J. J.; Maloney, J. M.; Chen, D.; Smith, J. F.; Bishop, S. R.; Tuller, H. L.; Van Vliet, K. J. Dynamic Chemical Expansion of Thin-Film Non-stoichiometric Oxides at Extreme Temperatures. *Nat. Mater.* **2017**, *16*, 749–754.
- (3) Garbayo, I.; Pla, D.; Morata, A.; Fonseca, L.; Sabaté, N.; Tarancón, A. Full Ceramic Micro Solid Oxide Fuel Cells: Towards More Reliable MEMS Power Generators Operating at High Temperatures. *Energy Environ. Sci.* **2014**, *7*, 3617–3629.
- (4) Sunarso, J.; Baumann, S.; Serra, J. M.; Meulenberg, W. A.; Liu, S.; Lin, Y. S.; Diniz da Costa, J. C. Mixed Ionic-Electronic Conducting (MIEC) Ceramic-Based Membranes for Oxygen Separation. *J. Membr. Sci.* **2008**, *320*, 13–41.
- (5) Perry, N. H.; Kim, J. J.; Bishop, S. R.; Tuller, H. L. Strongly Coupled Thermal and Chemical Expansion in the Perovskite Oxide System  $\text{Sr}(\text{Ti,Fe})\text{O}_{3-\alpha}$ . *J. Mater. Chem. A* **2015**, *3*, 3602–3611.
- (6) Bishop, S. R.; Tuller, H. L.; Kuru, Y.; Yildiz, B. Chemical Expansion of Nonstoichiometric  $\text{Pr}_{0.1}\text{Ce}_{0.9}\text{O}_{2-\delta}$ : Correlation With Defect Equilibrium Model. *J. Eur. Ceram. Soc.* **2011**, *31*, 2351–2356.
- (7) Mogni, L. V.; Prado, F. D.; Cuello, G. J.; Caneiro, A. Study of the Crystal Chemistry of the  $n = 2$  Ruddlesden-Popper Phases  $\text{Sr}_3\text{FeMO}_{6+\delta}$  ( $M = \text{Fe, Co, and Ni}$ ) Using *In Situ* High Temperature Neutron Powder Diffraction. *Chem. Mater.* **2009**, *21*, 2614–2623.
- (8) Atkinson, A.; Ramos, T. M. G. M. Chemically-Induced Stresses in Ceramic Oxygen Ion-Conducting Membranes. *Solid State Ionics* **2000**, *129*, 259–269.
- (9) Ahn, K.; Chung, Y.-C.; Yoon, K. J.; Son, J.-W.; Kim, B.-K.; Lee, H.-W.; Lee, J.-H. Lattice-Strain Effect on Oxygen Vacancy Formation in Gadolinium-Doped Ceria. *J. Electroceram.* **2014**, *32*, 72–77.
- (10) Kushima, A.; Yip, S.; Yildiz, B. Competing Strain Effects in Reactivity of  $\text{LaCoO}_3$  with Oxygen. *Phys. Rev. B: Condens. Matter Mater. Phys.* **2010**, *82*, 115435.
- (11) Han, J. W.; Yildiz, B. Enhanced One Dimensional Mobility of Oxygen on Strained  $\text{LaCoO}_3(001)$  Surface. *J. Mater. Chem.* **2011**, *21*, 18983–18990.
- (12) Yildiz, B. Stretching the Energy Landscape of Oxides—Effects on Electrocatalysis and Diffusion. *MRS Bull.* **2014**, *39*, 147–156.
- (13) Waser, R.; Dittmann, R.; Staikov, G.; Szot, K. Redox-Based Resistive Switching Memories - Nanoionic Mechanisms, Prospects, and Challenges. *Adv. Mater.* **2009**, *21*, 2632–2663.
- (14) Bishop, S. R.; Stefanik, T. S.; Tuller, H. L. Defects and Transport in  $\text{Pr}_x\text{Ce}_{1-x}\text{O}_{2-\delta}$ : Composition Trends. *J. Mater. Res.* **2012**, *27*, 2009–2016.
- (15) Chen, D.; Bishop, S. R.; Tuller, H. L. Praseodymium-Cerium Oxide Thin Film Cathodes: Study of Oxygen Reduction Reaction Kinetics. *J. Electroceram.* **2012**, *28*, 62–69.
- (16) Swallow, J. G.; Kim, J. J.; Kabir, M.; Smith, J. F.; Tuller, H. L.; Bishop, S. R.; Van Vliet, K. J. *Operando* Reduction of Elastic Modulus in  $(\text{Pr,Ce})\text{O}_{2-\delta}$  Thin Films. *Acta Mater.* **2016**, *105*, 16–24.
- (17) Marrocchelli, D.; Bishop, S. R.; Tuller, H. L.; Yildiz, B. Understanding Chemical Expansion in Non-stoichiometric Oxides: Ceria and Zirconia Case Studies. *Adv. Funct. Mater.* **2012**, *22*, 1958–1965.
- (18) Marrocchelli, D.; Bishop, S. R.; Tuller, H. L.; Watson, G. W.; Yildiz, B. Charge Localization Increases Chemical Expansion in Cerium-Based Oxides. *Phys. Chem. Chem. Phys.* **2012**, *14*, 12070–12074.
- (19) Kuru, Y.; Marrocchelli, D.; Bishop, S. R.; Chen, D.; Yildiz, B.; Tuller, H. L. Anomalous Chemical Expansion Behavior of  $\text{Pr}_{0.2}\text{Ce}_{0.8}\text{O}_{2-\delta}$  Thin Films Grown by Pulsed Laser Deposition. *J. Electrochem. Soc.* **2012**, *159*, F799–F803.
- (20) Sheth, J.; Chen, D.; Kim, J. J.; Bowman, W. J.; Crozier, P. A.; Tuller, H. L.; Misture, S. T.; Zdzieszynski, S.; Sheldon, B. W.; Bishop, S. R. Coupling of Strain, Stress, and Oxygen Non-stoichiometry in Thin Film  $\text{Pr}_{0.1}\text{Ce}_{0.9}\text{O}_{2-\delta}$ . *Nanoscale* **2016**, *8*, 16499–16510.
- (21) Grande, T.; Tolchard, J. R.; Selbach, S. M. Anisotropic Thermal and Chemical Expansion in Sr-Substituted  $\text{LaMnO}_{3+\delta}$ : Implications for Chemical Strain Relaxation. *Chem. Mater.* **2012**, *24*, 338–345.
- (22) Chen, X.; Grande, T. Anisotropic Chemical Expansion of  $\text{La}_{1-x}\text{Sr}_x\text{CoO}_{3-\delta}$ . *Chem. Mater.* **2013**, *25*, 927–934.
- (23) Chen, Q. N.; Adler, S. B.; Li, J. Imaging Space Charge Regions in Sm-Doped Ceria Using Electrochemical Strain Microscopy. *Appl. Phys. Lett.* **2014**, *105*, 201602.
- (24) Song, K.; Schmid, H.; Srot, V.; Gilardi, E.; Gregori, G.; Du, K.; Maier, J.; van Aken, P. A. Cerium Reduction at the Interface Between Ceria and Ytria-Stabilised Zirconia and Implications for Interfacial Oxygen Non-stoichiometry. *APL Mater.* **2014**, *2*, 032104.
- (25) Turner, S.; Lazar, S.; Freitag, B.; Egoavil, R.; Verbeeck, J.; Put, S.; Strauven, Y.; Van Tendeloo, G. High Resolution Mapping of Surface Reduction in Ceria Nanoparticles. *Nanoscale* **2011**, *3*, 3385–3390.
- (26) Hailstone, R. K.; DiFrancesco, A. G.; Leong, J. G.; Allston, T. D.; Reed, K. J. A Study of Lattice Expansion in  $\text{CeO}_2$  Nanoparticles by Transmission Electron Microscopy. *J. Phys. Chem. C* **2009**, *113*, 15155–15159.
- (27) Kim, Y.-M.; He, J.; Biegalski, M. D.; Ambaye, H.; Lauter, V.; Christen, H. M.; Pantelides, S. T.; Pennycook, S. J.; Kalinin, S. V.; Borisevich, A. Y. Probing Oxygen Vacancy Concentration and Homogeneity in Solid-Oxide Fuel-Cell Cathode Materials on the Subunit-Cell Level. *Nat. Mater.* **2012**, *11*, 888–894.
- (28) Sinclair, R. *In Situ* High-Resolution Transmission Electron Microscopy of Material Reactions. *MRS Bull.* **2013**, *38*, 1065–1071.
- (29) Borisevich, A. Y.; Chi, M.; Unocic, R. Functional Electron Microscopy for Electrochemistry Research: From the Atomic to the Micro Scale. *Electrochem. Soc. Interface* **2014**, *23*, 61–66.
- (30) Egerton, R. F. Electron Energy-Loss Spectroscopy in the TEM. *Rep. Prog. Phys.* **2009**, *72*, 016502.
- (31) Bowman, W. J.; March, K.; Hernandez, C. A.; Crozier, P. A. Measuring Bandgap States in Individual Non-stoichiometric Oxide Nanoparticles Using Monochromated STEM EELS: The Praseodymium-Ceria Case. *Ultramicroscopy* **2016**, *167*, 5–10.
- (32) Jang, J. H.; Kim, Y.-M.; He, Q.; Mishra, R.; Qiao, L.; Biegalski, M. D.; Lupini, A. R.; Pantelides, S. T.; Pennycook, S. J.; Kalinin, S. V.; Borisevich, A. Y. *In Situ* Observation of Oxygen Vacancy Dynamics and Ordering in the Epitaxial  $\text{LaCoO}_3$  System. *ACS Nano* **2017**, *11*, 6942–6949.
- (33) Hÿtch, M. J.; Snoeck, E.; Kilaas, R. Quantitative Measurement of Displacement and Strain Fields From HREM Micrographs. *Ultramicroscopy* **1998**, *74*, 131–146.
- (34) Gong, C.; He, K.; Robertson, A. W.; Yoon, E.; Lee, G.-D.; Warner, J. H. Spatially Dependent Lattice Deformations for Dislocations at the Edges of Graphene. *ACS Nano* **2015**, *9*, 656–662.
- (35) Chen, D.; Bishop, S. R.; Tuller, H. L. Non-stoichiometry in Oxide Thin Films: A Chemical Capacitance Study of the Praseodymium-Cerium Oxide System. *Adv. Funct. Mater.* **2013**, *23*, 2168–2174.
- (36) Sinclair, R.; Lee, S. C.; Shi, Y.; Chueh, W. C. Structure and Chemistry of Epitaxial Ceria Thin Films on Ytria-Stabilized Zirconia Substrates, Studied by High Resolution Electron Microscopy. *Ultramicroscopy* **2017**, *176*, 200–211.
- (37) Chen, C. H.; Kiguchi, T.; Saiki, A.; Wakiya, N.; Shinozaki, K.; Mizutani, N. Characterization of Defect Type and Dislocation Density in Double Oxide Heteroepitaxial  $\text{CeO}_2/\text{YSZ}/\text{Si}(001)$  Films. *Appl. Phys. A: Mater. Sci. Process.* **2003**, *76*, 969–973.
- (38) Gao, P.; Wang, Z.; Fu, W.; Liao, Z.; Liu, K.; Wang, W.; Bai, X.; Wang, E. *In Situ* TEM Studies of Oxygen Vacancy Migration for

Electrically Induced Resistance Change Effect in Cerium Oxides. *Micron* **2010**, *41*, 301–305.

(39) Cooper, D.; Baumer, C.; Bernier, N.; Marchewka, A.; La Torre, C.; Dunin-Borkowski, R. E.; Menzel, S.; Waser, R.; Dittmann, R. Anomalous Resistance Hysteresis in Oxide ReRAM: Oxygen Evolution and Reincorporation Revealed by *In Situ* TEM. *Adv. Mater.* **2017**, *29*, 1700212.

(40) Crozier, P. A.; Wang, R.; Sharma, R. *In Situ* Environmental TEM Studies of Dynamic Changes in Cerium-Based Oxides Nanoparticles During Redox Processes. *Ultramicroscopy* **2008**, *108*, 1432–1440.

(41) Bowman, W. J.; Zhu, J.; Sharma, R.; Crozier, P. A. Electrical Conductivity and Grain Boundary Composition of Gd-doped and Gd/Pr Co-doped Ceria. *Solid State Ionics* **2015**, *272*, 9–17.

(42) Sun, L.; Marrocchelli, D.; Yildiz, B. Edge Dislocation Slows Down Oxide Ion Diffusion in Doped CeO<sub>2</sub> by Segregation of Charged Defects. *Nat. Commun.* **2015**, *6*, 6294.

(43) Chen, D.; Tuller, H. L. Voltage-Controlled Nonstoichiometry in Oxide Thin Films: Pr<sub>0.1</sub>Ce<sub>0.9</sub>O<sub>2-δ</sub> Case Study. *Adv. Funct. Mater.* **2014**, *24*, 7638–7644.

(44) López-Cartes, C.; Bernal, S.; Calvino, J. J.; Cauqui, M. A.; Blanco, G.; Pérez-Omil, J. A.; Pintado, J. M.; Helveg, S.; Hansen, P. L. *In Situ* Transmission Electron Microscopy Investigation of Ce(IV) and Pr(IV) Reducibility in a Rh (1%)/Ce<sub>0.8</sub>Pr<sub>0.2</sub>O<sub>2-x</sub> Catalyst. *Chem. Commun.* **2003**, 644–645.

(45) Sameshima, S.; Kawaminami, M.; Hirata, Y. Thermal Expansion of Rare-Earth-Doped Ceria Ceramics. *Nippon Seramikusu Kyokai Gakujutsu Ronbunshi* **2002**, *110*, 597–600.

(46) Hayashi, H.; Saitou, T.; Maruyama, N.; Inaba, H.; Kawamura, K.; Mori, M. Thermal expansion Coefficient of Ytria Stabilized Zirconia for Various Ytria Contents. *Solid State Ionics* **2005**, *176*, 613–619.

(47) Bishop, S. R.; Stefanik, T. S.; Tuller, H. L. Electrical Conductivity and Defect Equilibria of Pr<sub>0.1</sub>Ce<sub>0.9</sub>O<sub>2-δ</sub>. *Phys. Chem. Chem. Phys.* **2011**, *13*, 10165–10173.

(48) Maicaneanu, S. A.; Sayle, D. C.; Watson, G. W. Evolution and Atomistic Structure of Dislocations Defects and Clusters Within CeO<sub>2</sub> Supported on ZrO<sub>2</sub>. *Chem. Commun.* **2001**, 289–290.

(49) Jia, B. W.; Tan, K. H.; Loke, W. K.; Wicaksono, S.; Yoon, S. F. Formation of Periodic Interfacial Misfit Dislocation Array at the InSb/GaAs Interface via Surface Anion Exchange. *J. Appl. Phys.* **2016**, *120*, 035301.

(50) Huang, S. H.; Balakrishnan, G.; Khoshakhlagh, A.; Jallipalli, A.; Dawson, L. R.; Huffaker, D. L. Strain Relief by Periodic Misfit Arrays for Low Defect Density GaSb on GaAs. *Appl. Phys. Lett.* **2006**, *88*, 131911.

(51) Kim, S. I.; Lee, K. H.; Mun, H. A.; Kim, H. S.; Hwang, S. W.; Roh, J. W.; Yang, D. J.; Shin, W. H.; Li, X. S.; Lee, Y. H.; Snyder, G. J.; Kim, S. W. Dense Dislocation Arrays Embedded in Grain Boundaries for High-Performance Bulk Thermoelectrics. *Science* **2015**, *348*, 109–114.

(52) Marrocchelli, D.; Sun, L.; Yildiz, B. Dislocations in SrTiO<sub>3</sub>: Easy to Reduce but Not so Fast for Oxygen Transport. *J. Am. Chem. Soc.* **2015**, *137*, 4735–4748.

(53) Ding, Y.; Chen, Y.; Pradel, K. C.; Liu, M.; Wang, Z. L. *In-Situ* Transmission Electron Microscopy Study of Oxygen Vacancy Ordering and Dislocation Annihilation in Undoped and Sm-Doped CeO<sub>2</sub> Ceramics During Redox Processes. *J. Appl. Phys.* **2016**, *120*, 214302.

(54) Kakihana, M.; Yoshimura, M. Synthesis and Characteristics of Complex Multicomponent Oxides Prepared by Polymer Complex Method. *Bull. Chem. Soc. Jpn.* **1999**, *72*, 1427–1443.

(55) Giannuzzi, L. A.; Stevie, F. A., Eds. *Introduction to Focused Ion Beams: Instrumentation, Theory, Techniques and Practice*; Springer, 2005; Chapter 10.

(56) Graff, A.; Simon, M.; Altmann, F. Using Enhanced SE Signal in the SEM for TEM Sample Thickness Determination. *Microsc. Microanal.* **2007**, *13*, 98–99.

(57) Mitchell, D. R. G. DiffTools: Electron Diffraction Software Tools for DigitalMicrograph™. *Microsc. Res. Tech.* **2008**, *71*, 588–593.

(58) Preibisch, S.; Saalfeld, S.; Tomancak, P. Globally Optimal Stitching of Tiled 3D Microscopic Image Acquisitions. *Bioinformatics* **2009**, *25*, 1463–1465.

(59) Schindelin, J.; Arganda-Carreras, I.; Frise, E.; Kaynig, V.; Longair, M.; Pietzsch, T.; Preibisch, S.; Rueden, C.; Saalfeld, S.; Schmid, B.; Tinevez, J. Y.; White, D. J.; Hartenstein, V.; Eliceiri, K.; Tomancak, P.; Cardona, A. Fiji: An Open-Source Platform for Biological-Image Analysis. *Nat. Nat. Methods* **2012**, *9*, 676–682.

(60) Schneider, C. A.; Rasband, W. S.; Eliceiri, K. W. NIH Image to ImageJ: 25 Years of Image Analysis. *Nat. Methods* **2012**, *9*, 671–675.

(61) Hovden, R.; Cueva, P.; Mundy, J. A.; Muller, D. A. The Open-Source Cornell Spectrum Imager. *Microsc. Microsc. Today* **2013**, *21*, 40–44.

(62) Efron, B. *Bootstrap Methods: Another Look at the Jackknife*. In *Breakthroughs in Statistics*; Kotz, S., Johnson, N. L., Eds.; Springer, 1992.